REPORT DOCUMENTATION PAGE

Form Approved OMB NO. 0704-0188

1. REPORT DATE (DD-MM-YYYY)	2. REPORT TYPE	3. DATES COVERED (From - To)
	New Reprint	-

4. TITLE AND SUBTITLE

Elimination of speckle and target orientation requirements in millimeter-wave active imaging by modulated multimode mixing illumination

5a. CONTRACT NUMBER	W911NF-09-1-0428
5b. GRANT NUMBER	
5c. PROGRAM ELEMENT NUMBER	611102
5d. PROJECT NUMBER	
5e. TASK NUMBER	
5f. WORK UNIT NUMBER	

6. AUTHORS

Jennifer A. Holt, Mark A. Patrick, Colin D. Joye, Frank C. De Lucia

7. PERFORMING ORGANIZATION NAMES AND ADDRESSES

Ohio State University Research Foundation
Office of Sponsored Programs
1960 Kenny Rd.
Columbus, OH 43210 -1063

8. PERFORMING ORGANIZATION REPORT NUMBER

9. SPONSORING/MONITORING AGENCY NAME(S) AND ADDRESS(ES)

U.S. Army Research Office
P.O. Box 12211
Research Triangle Park, NC 27709-2211

10. SPONSOR/MONITOR'S ACRONYM(S)
ARO

11. SPONSOR/MONITOR'S REPORT NUMBER(S)
56039-MS.36

12. DISTRIBUTION AVAILIBILITY STATEMENT

Approved for public release; distribution is unlimited.

13. SUPPLEMENTARY NOTES

The views, opinions and/or findings contained in this report are those of the author(s) and should not contrued as an official Department of the Army position, policy or decision, unless so designated by other documentation.

14. ABSTRACT

Active imaging can provide significantly larger signal margins in the millimeter-wave spectral region than passive imaging, especially indoors - an important application for which there is no cold sky illumination. However, coherent effects, such as speckle, negate much of this advantage by destroying image clarity and target recognition. Moreover, active imaging demonstrations often use strategically chosen target orientations to optimally reflect power from the active illuminator back to the imaging receiver. In this paper we will discuss and show

15. SUBJECT TERMS

millimeter-wave, imaging, speckle

16. SECURITY CLASSIFICATION OF:			17. LIMITATION OF ABSTRACT	15. NUMBER OF PAGES	19a. NAME OF RESPONSIBLE PERSON
a. REPORT	b. ABSTRACT	c. THIS PAGE			Frank De Lucia
UU	UU	UU	UU		19b. TELEPHONE NUMBER: 410-306-0884

Report Title

Elimination of speckle and target orientation requirements in millimeter-wave active imaging by modulated multimode mixing illumination

ABSTRACT

Active imaging can provide significantly larger signal margins in the millimeter-wave spectral region than passive imaging, especially indoors - an important application for which there is no cold sky illumination. However, coherent effects, such as speckle, negate much of this advantage by destroying image clarity and target recognition. Moreover, active imaging demonstrations often use strategically chosen target orientations to optimally reflect power from the active illuminator back to the imaging receiver. In this paper we will discuss and show experimental results for a new active imaging approach that largely eliminates coherent effects and the need for optimized target orientation. The work described uses a synthesized harmonic multiplier chain to drive a 5 W EIK at 218.4 GHz, a mechanical mode mixer to illuminate and modulate many modes, and a heterodyne receiver coupled into a 60 cm scanning mirror. Large signal margins were obtained in this ~50 m range work, showing paths to imaging at ~ 1 km, imaging with considerably less powerful illuminators, and the use of focal plane arrays.

REPORT DOCUMENTATION PAGE (SF298)
(Continuation Sheet)

Continuation for Block 13

ARO Report Number 56039.36-MS
Elimination of speckle and target orientation req ...

Block 13: Supplementary Note

Approved for public release; distribution is unlimited.

Elimination of speckle and target orientation requirements in millimeter-wave active imaging by modulated multimode mixing illumination

Mark A. Patrick,[1] Jennifer A. Holt,[1] Colin D. Joye,[2] and Frank C. De Lucia[1,*]

[1]*Physics Department, Ohio State University, Columbus, Ohio 43210, USA*
[2]*Code 6843, U.S. Naval Research Laboratory, Washington DC 20375, USA*
**Corresponding author: fcd@mps.ohio-state.edu*

Received April 26, 2012; revised August 29, 2012; accepted August 31, 2012;
posted October 24, 2012 (Doc. ID 167502); published November 28, 2012

Active imaging can provide significantly larger signal margins in the millimeter-wave spectral region than passive imaging, especially indoors—an important application for which there is no cold sky illumination. However, coherent effects, such as speckle, negate much of this advantage by destroying image clarity and target recognition. Moreover, active imaging demonstrations often use strategically chosen target orientations to optimally reflect power from the active illuminator back to the imaging receiver. In this paper we will discuss and show experimental results for a new active imaging approach that largely eliminates coherent effects and the need for optimized target orientation. The work described uses a synthesized harmonic multiplier chain to drive a 5 W extended interaction klystron at 218.4 GHz, a mechanical mode mixer to illuminate and modulate many modes, and a heterodyne receiver coupled into a 60 cm scanning mirror. Large signal margins were obtained in this ~50 m range work, showing paths to imaging at ~1 km, imaging with considerably less powerful illuminators, and the use of focal plane arrays.

OCIS codes: 030.6140, 110.6795, 350.4010.

1. INTRODUCTION

Imaging in the millimeter- and submillimeter-wave (hereafter referred to as the millimeter-wave) spectral region has long been a topic of interest [1–13]. Much of this interest results because radiation here provides a useful compromise between penetration and angular resolution.

Broadly speaking, millimeter-wave imaging can be divided into passive and active imaging. Passive imaging is particularly advantageous outdoors where cold sky illumination can provide significant temperature contrast, especially at the longer wavelengths where atmospheric transmission is greater. However, for most indoor and many outdoor applications active illumination is advantageous to compensate for low thermal contrast [5,9,14,15]. But active imaging comes with its own challenges: the need to deal with coherent effects (such as speckle), orientation requirements for targets, and decreasing sensitivity with increased range [6,7,9,10,16]. As a result, signal analysis and processing approaches (often tuned for the recognition of specific targets) are often employed to enable recognition for visually challenged active images [9,14].

Figure 1 illustrates many of these points for images recorded near 650 GHz from a distance of ~2 m. Whereas the passive image [12] looks much like an optical black and white photo of a diffuse object, the active image [6] is dominated by the strong specular reflections from the bridge of the forehead and cheeks (and the near absence of signal from the nonperpendicular parts of the cheeks). The beard of the active image is dominated by speckle, whereas the hair in the passive image is not.

While there has been considerable discussion of terahertz time domain spectroscopy and other proximate imaging approaches [17,18], techniques based on electronic technologies have proved to be more appropriate for nonproximate imaging [4,13]. The three-dimensional holographic systems (operating near 30 GHz, on the edge of the millimeter-wave region) that are being deployed for airport security are particularly interesting and serve as a model of strategies for relatively short range [3]. Likewise, most demonstrations of active imaging have been at relatively short (~2 m) distances [5,6,19,20], although there are notable exceptions [21].

In this paper, we will describe active imaging with a 218.4 GHz system in the atrium of the Physics Building at Ohio State University. This atrium has a scale dimension of 50 m and can serve as a surrogate for an "urban canyon." We will describe a compact method that can eliminate in active imaging both the aforementioned coherent effects and the need to strategically orient specular targets. The resultant images are similar to passive images (e.g., the passive image in Fig. 1), but with significantly larger signal margins. This approach fills many of the modes of a scenario with modulated mode mixed radiation from a coherent electronic source. Because it does so in a manner that both destroys the coherence of the illumination and the requirements for special target orientations, the resultant image is closely related to that which would result from illumination with a very hot blackbody.

The numerical enabler of this approach is that 1 mW of power in a single mode of bandwidth 1 MHz corresponds to a brightness temperature of 10^{14} K. Thus, modest amounts

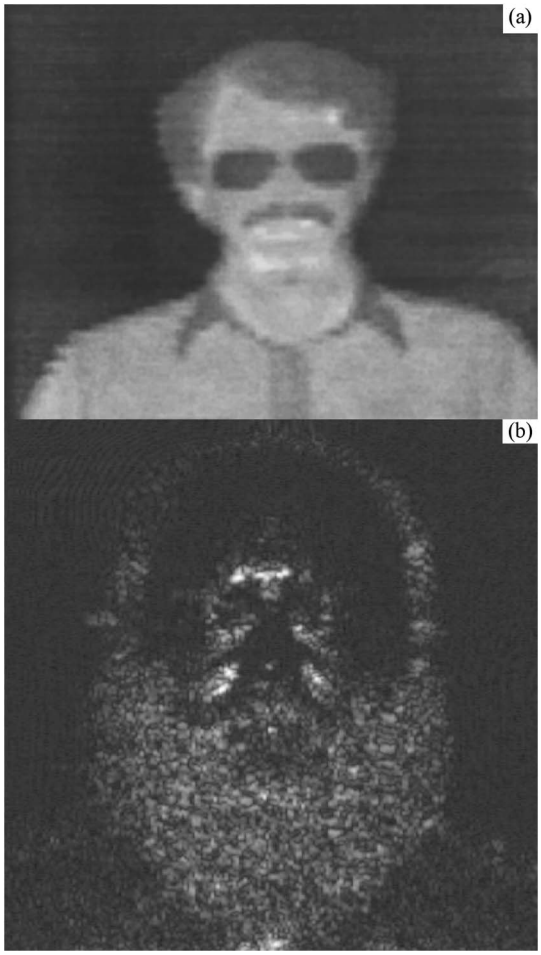

Fig. 1. (a) Indoor image of a face made with a passive bolometer system centered on ~650 GHz and (b) an image of a face made with an active illuminator and heterodyne receiver at 632 GHz.

of power can correspond to very hot blackbody temperatures even when distributed over many modes. We show that a 5 W extended interaction klystron (EIK) vacuum electronic source provides substantially more power than required in the Physics atrium and that extensions to considerably longer ranges are feasible. We will also discuss compact illumination strategies that will aid in the generalization of this approach to a variety of scenarios of interest.

2. BACKGROUND

A. Active and Passive Imaging: Detectors and Figures of Merit

Thermal radiation provides the signal as well as the noise in passive systems, and as a result the bandwidths of receivers are optimized differently for passive and active imagers. Because we seek to obtain active images that have many of the characteristics of passive images, we will start by first considering this issue and the figures of merit that characterize receivers and detectors.

1. Heterodyne and Square-Law Figures of Merit

From a photon flux noise point of view, there is no difference between heterodyne and square-law detectors. If a heterodyne system views the same bandwidth b as a square-law detector, ideal implementations of either have the same noise performance. However, the implementations are very different and the figures of merit that have evolved reflect this.

For both, the integration bandwidth B can easily be adjusted in postprocessing and this bandwidth is not included in the figure of merit. For a square-law detector a figure of merit, the noise equivalent power (NEP), can be defined so that the noise power of a detector referenced to its input is

$$P_n = \mathrm{NEP} \cdot B^{1/2}. \tag{1}$$

If the NEP of such a system is limited by the fluctuations in the photons from the target, expressions can be developed that relate the NEP to the temperature of the target, the area of the detector element, and the bandwidth observed [22,23]. For a single mode receiver in the long wavelength limit with a maximum detector response frequency $\nu_{\max}$, the more complicated relations for the entire blackbody spectrum reduce to [24]

$$P_n \sim kT(B\nu_{\max})^{1/2} = kT\nu_{\max}\left(\frac{B}{\nu_{\max}}\right)^{1/2} \tag{2}$$

or

$$\mathrm{NEP} = kT\nu_{\max}^{1/2}. \tag{3}$$

However, in room temperature square-law detectors (and even most cryogenic detectors except those that operate at very low temperatures) the detector responsivity is such that they are dominated by internal rather than photon noise and the NEP for most square-law detectors is several orders of magnitude higher.

In contrast, heterodyne systems are characterized by their noise temperature T_n. With intermediate frequency (IF) bandwidth b (which sets the optical bandwidth) and integration bandwidth B, their noise power referenced to their input is

$$P_n = kT_n(Bb)^{1/2}, \tag{4}$$

and the minimum detectable temperature difference becomes

$$\Delta T = T_n\left(\frac{B}{b}\right)^{1/2}. \tag{5}$$

It is possible to introduce an NEP-like figure of merit, NEP′, as

$$P_n = kT_n(Bb)^{1/2} = \mathrm{NEP}'(Bb)^{1/2}. \tag{6}$$

Hence, NEP′ is effectively a noise temperature, scaled by k. Since NEP and NEP′ have fundamentally different units, clearly they are not a basis for comparison of detectors.

The reasons for these differing figures of merit is that typically a square-law detector has a bandwidth (set perhaps by optical filters or mode-coupling considerations) that is not easily changed in electronics by the operator, whereas the IF bandwidth b of a heterodyne receiver is often easily adjustable. Consequently, the optical bandwidth of the square-law detector is built into its figure of merit (the NEP), whereas the figure of merit for the heterodyne receiver (its noise temperature) does not include optical bandwidth. Moreover, since the internal noise of most square-law detectors is dominant, their

optical bandwidth is not an important factor in their noise performance.

2. Numerical Examples

We can use

$$\mathrm{NEP}' b^{1/2} = \mathrm{NEP}_{\mathrm{equiv}} \tag{7}$$

to compare heterodyne and square-law detectors, but this comparison will be different if the system is optimized for broad optical bandwidth b for passive imaging, or for narrow optical bandwidth b for active imaging.

For a heterodyne receiver optimized for passive imaging with noise temperature of $T_n = 3000$ K (a bit high for 94 GHz) and a 10 GHz bandwidth,

$$\mathrm{NEP}_{\mathrm{equiv}} = 4 \cdot 10^{-15}\ \mathrm{W/Hz^{1/2}}. \tag{8}$$

For a square-law detector to reach this value requires a very good cryogenic detector, such as the 300 mK. ^{3}He refrigerated bolometer used to make the passive image in Fig. 1.

The comparison is different, however, for an active system whose receiver has a nominal bandwidth of 1 MHz because the $b^{1/2}$ factor in Eq. (7) changes the comparison by a factor of 100. Of equal importance, at room temperature it is much easier to approach (for both technical and fundamental reasons) the background noise limited case. For example, if we consider a room-temperature square-law detector with an NEP of 10^{-11} W/Hz$^{1/2}$, it is comparable to a heterodyne receiver whose bandwidth is 1 MHz with

$$T_n = \frac{\mathrm{NEP}'}{k} = \frac{\mathrm{NEP}_{\mathrm{equiv}}}{k b^{1/2}} \sim 10^9\ \mathrm{K}. \tag{9}$$

This results in a significantly larger ratio between the two detector approaches for active imaging than for the passive imaging example above. Thus, room-temperature square-law detectors start with a disadvantage as detectors for active systems. However, if sufficient illumination power is available, their simplicity makes them attractive, especially for focal plane arrays.

3. Thermal and Active Illumination Power

It is useful to note that a passive imager with 10 GHz bandwidth and a diffraction-limited 100×100 array receives $\sim 4 \times 10^{-7}$ W from a 300 K blackbody. This can be compared with the amount of power supplied to a target by an active illuminator. For example, in an experiment [5] with a 120×120 microbolometer array located 88 cm from the target and illuminated by ~1 W pulsed source (100 ns at an 83 kHz pulse repetition rate), each element received ~1 μW, or the entire array received ~10 mW, about three orders of magnitude higher than the passive power. If the imager is a single spot imager, all of the illumination power can be concentrated on one spot, in our example raising the illumination ratio to $\sim 10^7$.

For a comparison with passive systems, knowledge of the nature of the target is required. For optimally angled specular parts of the image, all of the power focused on the target is collected by the receiver; for nonoptimally oriented specular parts of the target, no power is collected by the receiver. For diffuse parts of the target, the power collected by the receiver is reduced by the fraction of the hemisphere viewed by the target occupied by the collection optics. Since 30 cm optics were used in this experiment at a distance of 88 cm, a reasonably large fraction was collected. However, at a longer range, this fraction will become small, illustrating the differing effects of range on active and passive sensors.

4. Consequences

Nonetheless, in this experiment with a complex target (a toy gun illuminated from three angles to minimize the need for special angles), the signal levels were dramatically higher than the thermal radiation from the target. This allowed the use of a microbolometer array with an NEP $\sim 10^{-10}$ W/Hz$^{1/2}$. Because the microbolometer array is orders of magnitude simpler and less expensive than heterodyne or arrays with active millimeter-wave amplifiers, this is an enormous advantage. Since the thermal signal level from any one of the pixels is less than 10^{-10} W, power associated with this active illumination was required for the use of this array.

However, cooling bolometers to cryogenic temperatures provides the sensitivity required for passive imaging. The passive image shown in Fig. 1 was made with a 0.3 K Si bolometer, and the noise in this system is dominated by scenario fluctuation, not receiver noise. This overkill was a result of the detector's availability, not a desire for practicality. A much more practical alternative, which both has a line array and operates at temperatures that can be reached without cryogens by use of a mechanical cooler, has been demonstrated and represents a development path to practical systems [25].

B. Active Systems and the Nature of Targets

1. Speckle

Because of their importance in optical systems, considerable attention has been paid to coherent effects, especially speckle [26,27]. Goodman [28–30] has shown that if it is possible to average N statistically independent fully developed speckle patterns, then the speckle contrast

$$C = \frac{\sigma}{\langle I \rangle} \tag{10}$$

can be reduced from 1 (i.e., where σ the standard deviation of the speckle intensity is equal to the average intensity $\langle I \rangle$) to $1/\sqrt{N}$. The issue then is how to implement in a practical way a system for which N is a large number and for which the N speckle patterns are uncorrelated. Additionally, in many, if not most, real imaging applications the images result from a combination of diffuse and specular reflections and Rician statistics need to be considered [31]. In Section 6 below, examples of Rician analyses of real images are presented.

Let us first consider frequency modulation as a means to provide the uncorrelated speckle patterns. We have shown that frequency modulation can effectively suppress coherent effects that are associated with standing waves between the target and imaging system [6], but in these cases the multiple paths that produce the interference patterns are macroscopic—typically meters and many thousands of wavelengths are involved. However, the interference path differences that lead to speckle are on the order of the roughness of the target, which is comparable to the wavelength in the terahertz region. Goodman has shown the fractional frequency variation required to get a speckle contrast C from surface scattering is

$$\frac{\delta\nu}{\nu} = \frac{\lambda}{\sigma_h}\sqrt{\frac{\frac{1}{C^4}-1}{8\pi^2}}, \tag{11}$$

where σ_h is the standard deviation of surface height. To reduce C to ~0.1 at $\lambda = 1$ mm with $\sigma_h \sim 1$ mm, the required fractional modulation would be 1000%. A corollary of this result is that schemes based on combining images taken at several microwave wavelengths within a waveguide band will have little effect. In Section 3, we show that this expectation of small speckle reduction is confirmed.

Angular diversity provides another path toward uncorrelated speckle patterns. Let us consider the photons collected for a single diffraction-limited pixel by an observing system with optics of diameter D_o, located a distance r_{to} from the target. The area of the spot size on the target of this observing system (which defines a single mode) is

$$A_S = \left(\frac{\lambda r_{to}}{D_o}\right)^2. \tag{12}$$

This area views [32]

$$N = \frac{2\pi A_S}{\lambda^2} = 2\pi\left(\frac{r_{to}}{D_o}\right)^2 \tag{13}$$

modes in 2π steradians. If all of these modes are excited sequentially by the same coherent source, the speckle pattern for each is developed from incoherent photons and averaging over these speckle patterns will reduce the speckle contrast by $\sqrt{N}$. The scale of the atrium in our experiment is $r_{to} \sim 50$ m and $D_o = 1$ m, yielding $N = 5000\pi$. A similar result is obtained by Goodman for the conjugate problem of the images being formed by the illuminator [30]. Clearly in this blackbody limit, there are many modes available and it will be possible to consider a wide variety of scenarios for which significant speckle reduction is possible.

2. Mirrors, Scatters, and Speckle

Figure 2 shows a controlled experiment in which a square mirror (mounted on a post) was covered on the left and right with Eccosorb and a thin scarf was placed over the top half of the combination. The upper panel shows an image taken from ~1.5 m, normal to the mirror, with a 632 GHz active imaging system, which we have previously described [6]. The image in the lower panel is of the same target, rotated by 20°.

The image of the Eccosorb on the left and right of the target is essentially unchanged with rotation and is dominated by the speckle associated with the diffuse reflection into a large solid angle. Careful inspection will show that the details of the speckle have changed. However, the bottom half of the mirror changes from returning essentially all of the active probe radiation to returning none of it because of the rotation. A more careful and quantitative analysis of the mirror in the lower image shows that it returns a signal from the diffuse background that it images. It is interesting that while the thin scarf provides almost no attenuation in the path to the normal mirror, that its return signal and speckle are hardly distinguishable from the Eccosorb when rotated by 20°.

As the range is increased, at some point the resolution of the imaging system becomes such that the mirror changes from being a 100% reflector (independent of range), to a radar-like point (whose return signal varies as $1/r^4$). Moreover, the requirement for angular alignment Θ_{sp}

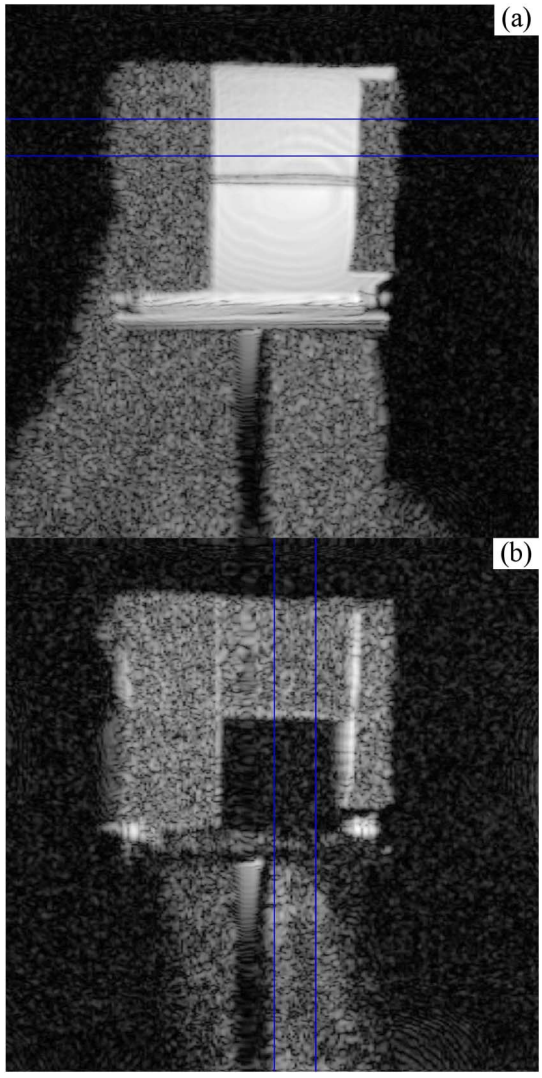

Fig. 2. (Color online) Mirror covered with Eccosorb on left and right, with a thin scarf on top. In (a) the mirror is normal to the optical axis and in (b) the mirror is rotated by 20°.

$$2\Theta_{sp} \sim \frac{D_o}{r} \tag{14}$$

for the specular return increases inversely with range [20].

As long as the diffuse Eccosorb is large enough to be imaged by the system, its return will vary by $1/r^2$, before becoming $1/r^4$ in the radar limit. In fact, the reason that the uncovered mirror rotated by 20° appears black is because of this $1/r^2$ effect for the more distant background it images. An important conclusion is that the more complex images that we will next consider will be strong functions of range, with specular reflections becoming less important than diffuse reflections at longer range.

3. A More Complex Target

The upper panel of Fig. 3 shows a 632 GHz image of a toy gun placed atop an optical breadboard, with holes separated by 2.54 cm. Because this target was oriented perpendicularly to the line of sight, it was dominated by strong, speckle-free,

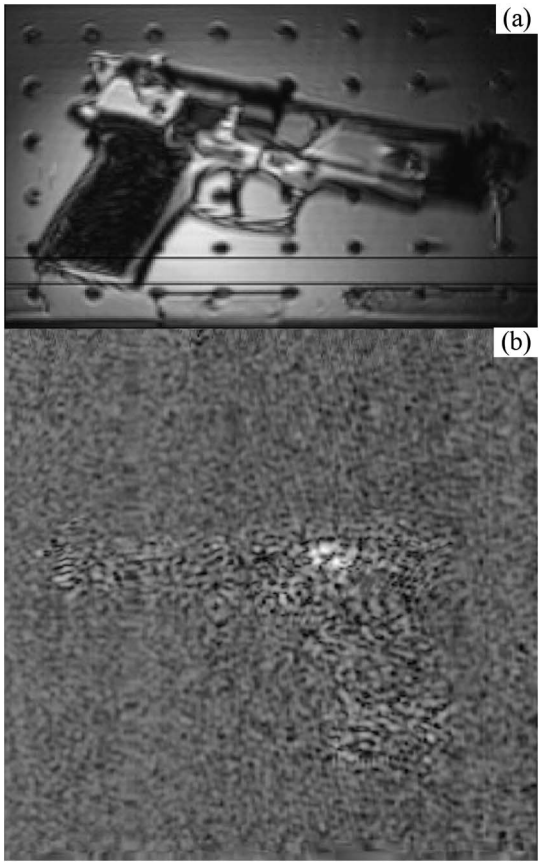

Fig. 3. (a) Image of an optimally oriented toy gun placed atop an optical breadboard with hole spacing of 2.54 cm and (b) an image of the same gun located in a reflective enclosure to provide illumination in many modes from many angles.

specular reflections. However, if the target was rotated, the image strength dropped by 10–40 dB and was dominated by a few glints [6]. In an attempt to remove this special angle requirement, the target was placed in a $4' \times 4' \times 8'$ enclosure and randomly illuminated by the many reflections within the box. The image in the lower panel of Fig. 3 resulted. Since there was no longer an optimal orientation, the strategic orientation requirement was removed—a good thing. But since the optimum orientation for the specular image in the upper panel produced the strong specular reflection that made it stand out was removed, the image now virtually disappeared into the speckle background, even though in the lower panel the background for the target was Eccosorb.

An experiment in which a Ka-band (26.5–40 GHz) noise source is used to illuminate a human size chamber through many holes and angles has also been reported [33]. The combination of the more specular reflections at longer wavelength, illumination from a fraction of the solid angle, and a larger target contrast provides a distinct outline of the target and reduces the visual impact of the speckle from that shown in the lower panel of Fig. 3.

3. PREVIOUS RESULTS

A. Experiments

1. Frequency Modulation

Equation (11) showed that for significant speckle contrast reduction very large fractional modulations (often exceeding 100%) are required. A number of experiments bear out this prediction. For example, a multispectral technique has been proposed and demonstrated using five frequencies in the 75–110 GHz region ($\lambda \sim 3$ mm) on five metal strips with interface steps of 2.5–5 mm [9]. While the coherence effects associated with the active illumination were reduced, with the 35% bandwidth, coherence still significantly impacted the resultant images. As a result of these limitations, mathematical algorithms for target recognition were proposed [9]. In another experiment several images were obtained in the 40–200 GHz range [34]. While this represents a large fractional change in frequency, the differences in the diffraction-limited resolution over this range raises the challenging question of how these images might be combined for reduction of coherent effects.

These results show how much more challenging it is to use frequency modulation for speckle reduction than for elimination of coherent effects related to macroscopic standing waves. For example, it was possible to eliminate the coherent effects caused by source-to-target standing waves with a frequency modulation of only $\Delta\nu/\nu \approx 10^{-4}$ [20].

2. Hadamard Phase Modulation

Hadamard phase pattern illumination has been studied in some detail as a means for speckle reduction in active millimeter wave images [11], but the improvements available are modest and at some sacrifice in image resolution. For example Jaeger *et al.* have reported an experiment in which a Hadamard diffuser resulted in a 50% reduction in speckle [10]. Ocket *et al.* have shown that the efficiency of this approach is more limited in millimeter-wave systems than might be expected from calculations based on Fourier optics [7,35], and Koers *et al.* [11] have shown that there are more restrictions on applying the Hadamard approach at millimeter rather than optical wavelengths.

3. Angular Diversity

The speckle pattern is randomized when the viewing or illumination angle changes by an angle

$$\theta \sim \frac{D_o}{r_{to}}, \tag{15}$$

where D_o is the diameter of the observing optics and r_{to} is the distance from the target to the observing optics [20,30,31]. This is essentially the angle between diffraction-limited modes that determines the statistical independence of the photons. Figure 4 shows experimental results that confirm this expectation [20] by its reduction of the speckle contrast ratio to

$$C = 1/\sqrt{16} = 0.25. \tag{16}$$

This angular diversity also reduces the need for strategic angular alignment to enhance the strong contributions of specular components to images. Jaegar *et al.* [10] have implemented a multiangle system at 94 GHz that allowed viewing from five angles over 20° and achieves a speckle contrast on two metal strips of 0.754 and note that this averaged image was “still rich with speckle.”

B. Theory and Signal Processing

Modeling of these coherent phenomena has been challenging and this has an impact on theoretical evaluation of speckle

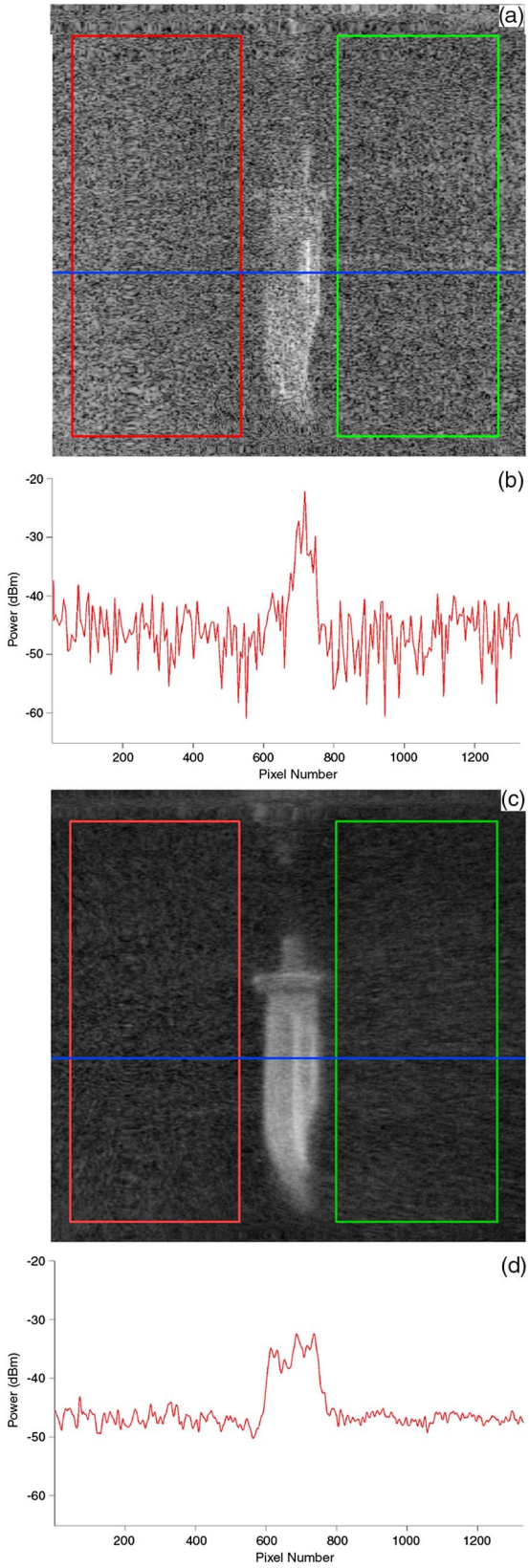

Fig. 4. (Color online) (a) Image of a knife under a thin brown robe at 632 GHz. (c) Co-added image of a knife taken at 16 independent angles as defined by Eq. (15). The quantitative traces below each image show the signal along the blue line in each image. These graphs show that the speckle contrast noise is reduced by $(16)^{1/2} = 4$ by the averaging over the 16 independent images. A more formal analysis of the speckle in the red (left) and green (right) boxes is presented in Subsection 6.B.

reduction techniques. For example, Qi *et al.* [36] have considered requirements for accurate modeling and found that approaches based on Fourier optics (frequency domain) calculations are not as accurate as calculations in the spatial domain. This is especially true when surface roughness (and the resulting speckle and other coherent effects) is important.

Because of the challenges of experimentally implementing these speckle reduction strategies or of their limitations, considerable attention has been paid to signal processing techniques, with emphasis on improved recognition rather than visually improved images. As an example, in a proximate imaging experiment for the detection of landmines, a principal component analysis was used in an experiment in which images taken at 51 different frequencies in the 94–140 GHz band were used [19]. Since the fractional bandwidth was too small to eliminate the coherent effects, a multiple component analysis was used as an aid. In this viewing geometry the resultant lowest-order component (which contained the main specular reflection) was reasonably free of coherent clutter. However, the higher components (which show more of the detail of the image of the mine) showed considerable coherent phenomena. Additionally, they showed that unless the earth above the landmine was flat, coherent clutter obscured the target image. These results are consistent with the bandwidth requirements as expressed in Eq. (11), in the dominance of speckle-free specular reflections in normal viewing geometries, and of the impact of clutter from textured obscuring materials as shown in Fig. 4.

4. MODULATED MULTIMODE MIXING

In this section we will develop some of the foundations of modulated multimode mixing and in the following section show experimental results. We seek to use appropriately modulated and focused radiation from electronic sources to produce very hot, incoherent "blackbody" radiation to make passive-like images (which do not exhibit either coherent effects or require special angle target orientations). In Section 7, we will consider extensions to longer ranges, including consideration of alternative illumination strategies that suppress speckle and other coherent effects without the requirement of filling an enclosed volume with radiation.

A. Modes and Angles

Let us first assume that all of the power P of an electronic source is placed in a single mode and observed for a time defined by an optical bandwidth b. Then

$$T_{\text{eff}} = \frac{P}{kb}, \tag{17}$$

with $P = 1$ mW and $b = 1$ MHz, $T_{\text{eff}} \sim 10^{14}$ K. Other useful reference points include 10 W in 100 Hz and 1 mW in 10 GHz, which yield effective temperatures of 10^{22} K and 10^{10} K, respectively. Clearly, active illumination is orders of magnitude hotter than passive illumination, but the temperature can vary considerably.

The solid angle Ω of a single blackbody mode that an area A emits into it is [32]

$$\Omega = \frac{\lambda^2}{A}. \tag{18}$$

Thus, the area that illuminates the entire solid angle of a hemisphere is

$$A_{2\pi} = \frac{\lambda^2}{2\pi}. \tag{19}$$

The number of such independent illumination areas is

$$N_{2\pi} = \frac{2\pi\ell^2}{A_{2\pi}} = \frac{4\pi^2\ell^2}{\lambda^2} \tag{20}$$

with each radiating $P = kTb$.

Now assume that an external source of electromagnetic radiation of power P is inserted into the enclosure of length scale l and that it is uniformly distributed over the hemisphere and diffusely reflected from a surface of reflectivity $R \ll 1$. Then the single-mode power reflected by each $A_{2\pi}$ is

$$P_{sm} = PR\frac{A_{2\pi}}{2\pi l^2} = PR\frac{1}{4\pi^2}\frac{\lambda^2}{l^2} = kT_{\text{eff}}b, \tag{21}$$

where T_{eff} is the effective temperature of the surface if the power is within a bandwidth b.

From (20), for $\lambda = 1$ mm and $l = 100$ m

$$N_{2\pi} = 4\pi^2\frac{l^2}{\lambda^2} = 4\pi^2 \cdot 10^{10}. \tag{22}$$

Thus, if the single mode temperatures of a source of power 10 W and 1.0 mW for 1 MHz bandwidths are 10^{18} and 10^{14} respectively, and if the scattering reflectivity into these $4\pi^2 \times 10^{10}$ modes is $R = 0.1$, then the "blackbody" temperatures of the enclosure will be $\frac{10^7\ \text{K}}{4\pi^2}$ and $\frac{10^3\ \text{K}}{4\pi^2}$, respectively. If the target also has a reflectivity R, the target temperature coupled into the receiver mode is reduced by 10 to $\frac{10^6\ \text{K}}{4\pi^2}$ and $\frac{10^2\ \text{K}}{4\pi^2}$, respectively.

The 1 MHz bandwidth is somewhat arbitrary, but a lower limit of ~100 Hz would be set by frame rate considerations for the array. However, if we were using modulated mode mixing for speckle reduction and we wanted to reduce the speckle contrast by 100, this would require a minimum bandwidth of 1 MHz for the 100 Hz frame rate and the $N = 10^4$ images that would need to be averaged for the speckle reduction. However, the averaging over the 10^4 images would reduce the effective bandwidth back to 100 Hz. This averaging can either be done in software, or more simply by using an appropriate integration time at the detector.

5. EXPERIMENTAL

The images of Fig. 4 were made with a coaxial transmit and receive beams that imaged the same spot. Since in the experiments reported here we are not copropagating transmit and probe beams, the beam splitter of our earlier imaging experiment was replaced with a direct feed of the receiver, as shown in Fig. 5.

A. Transmitter

The transmitter is a single-mode transmitter consisting of a Virginia Diodes, Inc. (VDI) ×8 solid-state multiplier capable of 30 mW at 218.4 GHz feeding a 5 W 218.4 GHz EIK amplifier from CPI, Inc. (Model VKY2444). To illuminate a large area and provide a means for mode modulation, we first used a small horn to send the output of the EIK into an aluminum enclosure of size $24'' \times 18'' \times 56''$ with the top and one side made from polyethylene.

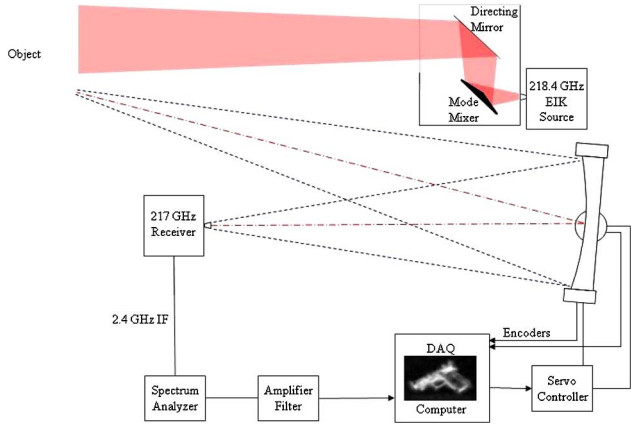

Fig. 5. (Color online) Mode mixing illumination and scanning receiver system. The power for the transmitter of this system originates is a 5 W EIK whose output illuminates a rotating rooftop mirror and reflects off of a second mirror that can be adjusted in angle, so as to illuminate many modes sequentially. The heterodyne receiver sits at the focus of a 60 cm diameter, 1 m focal length mirror, which is scanned to form the image.

B. Mode Mixer

To modulate the power in each illumination mode, the lower directional mirror in the transmitter enclosure was replaced by a mechanical mode mixer. The mode mixer consists of a 3 in. rotating disk with a raised center ridge, creating two faces with 15° slopes from horizontal. At a point in the revolution of the mode mixer, a set of illumination modes was created, and at that particular point a speckle pattern was created across the object (the atrium). The mode mixer was rotated at 6500 revolutions per minute. Below we will analyze the speckle patterns and the reduction that resulted from this mode averaging to determine how many independent modes were involved in the modulation.

C. Receiver

The imaging receiver consists of a spherical collecting mirror with a diameter of 0.6 m that focuses the incoming radiation onto a VDI heterodyne receiver with a local oscillator at 216.0 GHz. The resulting 2.4 GHz IF signal was amplified, filtered, and fed into a spectrum analyzer, used as a logarithmic detector. The resulting signal is digitized for image reconstruction after an integration bandwidth of 30 kHz. Since the receiver is a one pixel receiver, the spherical mirror is raster scanned over the scene of interest. With a diffraction-limited pixel dwell time of 10–60 ms, each picture took at least a few minutes to scan. However, if an array were used, near video frame rates are achievable with this pixel dwell time. In a typical scan of the Physics Building atrium, the image contained 200 by 200 diffraction-limited pixels and then displayed electronically as an 800 pixel by 800 pixel image, making each diffraction-limited spot size 4 image pixels by 4 image pixels. If the raster scan line misses an image pixel, the value of the pixel is linearly interpolated between the two surrounding scan lines. For a 60 ms diffraction-limited pixel dwell time, each image pixel has ~4 ms of integration time.

6. IMPACT OF MODULATED MODE MIXING ON IMAGE SPECKLE

A. Images

Figure 6 shows an optical image of the atrium of the OSU physics department. This is a considerably larger and more detailed scene than is typically used for demonstrations of millimeter-wave active images. The scale of the atrium is a length of about 50 m, a height of about 20 m, and a varying width of 7–15 m. The wall on the left is curved. At the far end are open staircases and platforms with glass partitions and railings.

One of the important issues is the location and mode mixing strategy of the active illuminator. In Section 4, it was assumed that all of the modes of an enclosure were illuminated equally and that they could be described by a temperature. However, especially at greater range and outdoors, one often seeks to optimize photon use while still illuminating enough modes so that speckle and the need for strategic target alignment can be eliminated or significantly reduced. In the work described in this section, we will work closer to the first limit. In the next section we will consider the latter limit.

The upper panel of Fig. 7 shows an image of the atrium with multimode illumination, but without modulated mode mixing. Because many modes are illuminated, the requirement for special angular alignment of the target is removed, but substantial speckle remains. The lower panel of Fig. 7 shows the same image, but with modulated mode mixing. For this work the illuminator was located on the floor near the right of the atrium, with the direct path of illumination from the transmitter to receiver blocked. For all of the ceiling beams, it can be seen that the bottoms of the beams are more strongly illuminated than their sides. Since many materials have similar diffuse scattering coefficients (compare, for example, the thin scarf and Eccoscorb in Fig. 2), this shadowing is important for image contrast. Similar effects are observed in the optical, for example along the terminator line of the Moon illuminated by the Sun.

A number of prominent features are associated with the open staircase in the far end of the atrium. From front to back are a glass front piece (topped by a metal railing), the up stairs going from right to left, a glass divider between the stairs, the up stairs going from left to right and the drywall of the atrium.

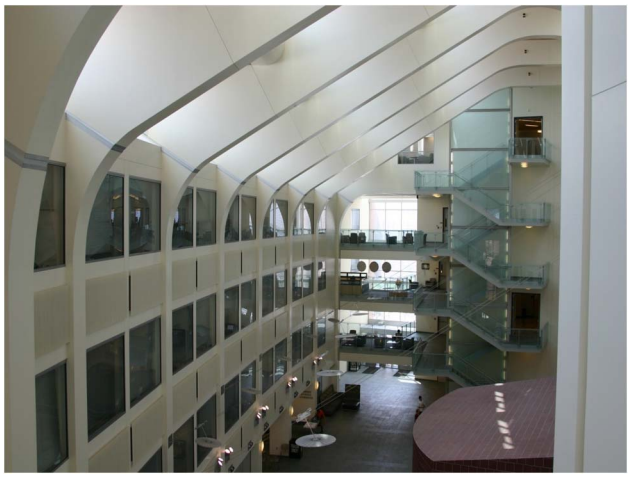

Fig. 6. (Color online) Optical image of the atrium of the Physics Building at Ohio State University.

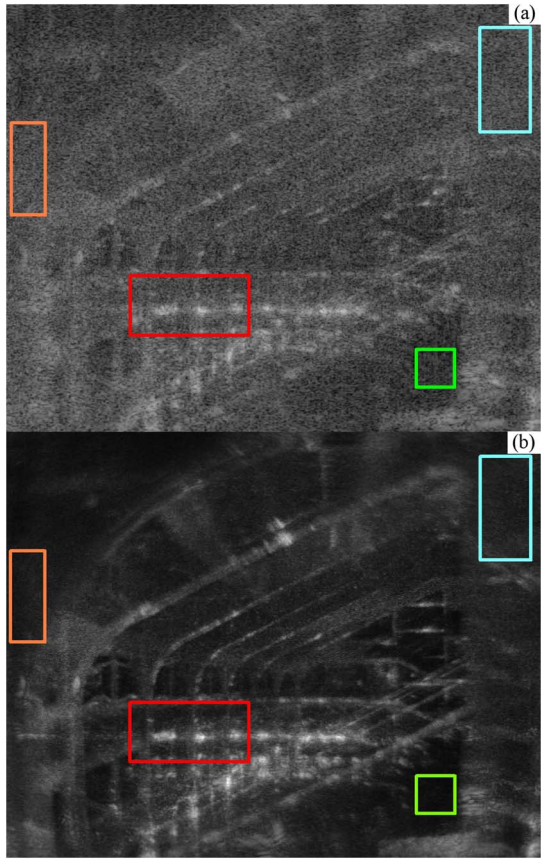

Fig. 7. (Color online) (a) 218.4 GHz image of the atrium of the Physics Building at Ohio State University with multimode illumination, but without modulated mode mixing and (b) with modulated mode mixing. The colored boxes show areas for which speckle statistics have been calculated.

While some of these features are observable in the upper panel, many more and additional detail are observable in the lower panel of Fig. 7. For example, the supports of the front stairs are clearly visible (as are the turning platforms). The handrails are also observable, but not as clearly. Additionally, lighting for the atrium is provided by the reflection of light from diffuser disks suspended by wires in the volume of the atrium. These wires are more easily visible in the millimeter image than in the optical image, appearing diagonally from the lower left to the middle right portion of the image.

B. Speckle Contrast

In Fig. 4 it was easy to visually observe the reduction of the speckle contrast because the image contained large uniform areas. It was also possible to show that that speckle noise was reduced by $N^{1/2}$, where N was the number of independent images in the average. However, in Fig. 7 the speckle size is comparable to the angular size of many of the small features in the atrium, and the evaluation of the speckle reduction requires a more formal approach.

1. Image of a Simple Object—a Knife Covered with Cloth

Let us start by using a more formal approach on the images in Fig. 4. Goodman's criteria for the independence of the speckle patterns [30] also concludes that of the 41 images taken across 41° there are 16 independent illumination angles. An image

that is the average of many speckle patterns will have an intensity distribution that follows a gamma density function of order N,

$$p_I(I) = \frac{N^N I^{N-1}}{\Gamma(N)\langle I\rangle^N} e^{-N\frac{I}{\langle I\rangle}}, \tag{23}$$

where N is the number of averaged speckle patterns and $\langle I\rangle$ is the mean intensity. The contrast of the image is reduced by the square root of the number of independent speckle patterns averaged in the image.

The intensity distribution for the region enclosed by the red box in upper panel of Fig. 4, containing no signal from the knife, only signal from the robe, is plotted and fit to Eq. (23) to determine N. After normalizing the intensity to the mean intensity, the fit returns $N = 1.32$, resulting in a speckle contrast factor of $C = 0.87$. The value $N = 1$ would result in the negative exponential curve that is characteristic of fully developed speckle. The region enclosed by the green box, also containing no signal from the knife, returns $N = 1.39$, resulting in a speckle contrast factor of $C = 0.85$. The experimental data points and the fitted curve are shown in Fig. 8.

2. Mode-Mixed Image of a Simple Object—a Knife Covered with Cloth

Figure 9 shows a similar comparison between experimental data points and the result of a fit to Eq. (23), except for the averaged image shown in the lower panel of Fig. 4. For the data contained by the red box, the fit returns $N = 15.46$, resulting in a contrast of $C = 0.25$. For the data contained by the green box, the fit returns $N = 17.38$, resulting in a contrast of $C = 0.24$. Averaging the two sides together

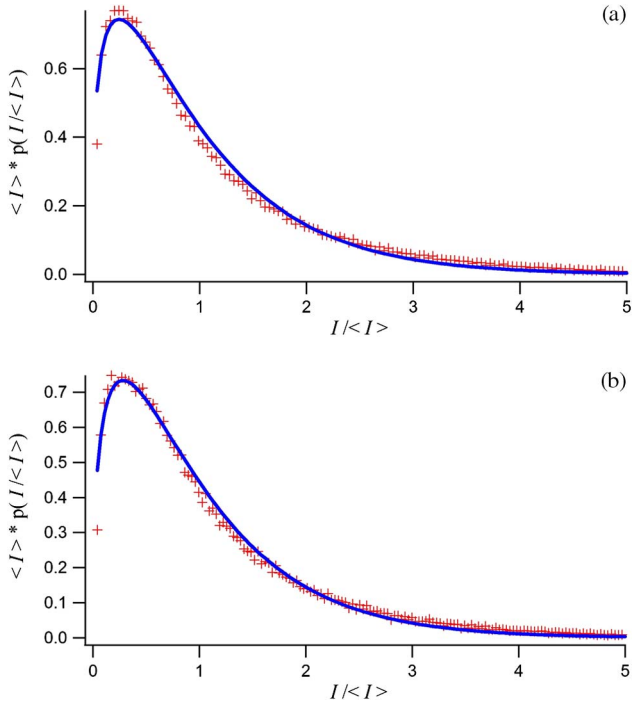

Fig. 8. (Color online) Experimental intensities of image points (red crosses) and curve fitted to Eq. (23) (blue line) for image points inside the red (left) box of the upper image of Fig. 4 and green (right) box, corresponding to (a) and (b) here.

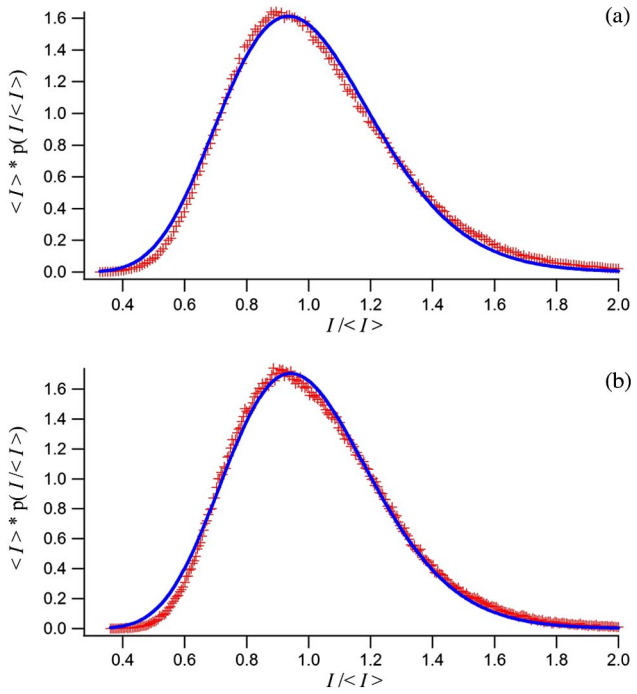

Fig. 9. (Color online) Experimental intensities of image points (red crosses) and curve fitted to Eq. (23) (blue line) for image points inside the red (left) box and green (right) box of the lower image of Fig. 4, corresponding to (a) and (b) here.

results in a value of $N = 16.4$, which closely agrees with the number of independent speckle patterns averaged. It is important to note that the gamma distribution of order N was derived assuming equal mean intensity from every averaged speckle pattern. This assumption is not exactly valid in our case since returned power varies modestly as a function of angle.

3. Image of a Complex Object—the Atrium of the OSU Physics Building

The gamma density function of Eq. (23) was first used to analyze the speckle at three areas of the unmodulated image of the Physics atrium shown in the upper panel of Fig. 7. The results are shown in Fig. 10. These areas were selected to have large, nearly uniform structures so that changes in scene geometry and reflectivity did not dominate the speckle statistics. The upper intensity distribution (orange box) is from a nearby wall (at ~10 m) made of painted drywall and returned a fit parameter $N = 3.63$. The middle intensity distribution (green box) is from a seminar room (at ~30 m) that is interior to the atrium and covered with rough tile and returned $N = 4.31$. The lower intensity distribution from a wall (at ~10 m), made of painted drywall, and returned $N = 3.84$. Since the contrast is inversely proportional to the square root of the fit parameter N, the average speckle contrast C of each of these images is 0.51.

However, as we have noted above, the images of the physics atrium are complex, not only because of the angular variation that forms the image, but also in the nature and variety of its reflection. For a surface that has a surface roughness that is less than a wavelength, the resulting reflection will be part specular and part diffuse. The resulting signal will not create the "fully developed speckle" pattern of Eq. (23), but will follow a modified Rician density function

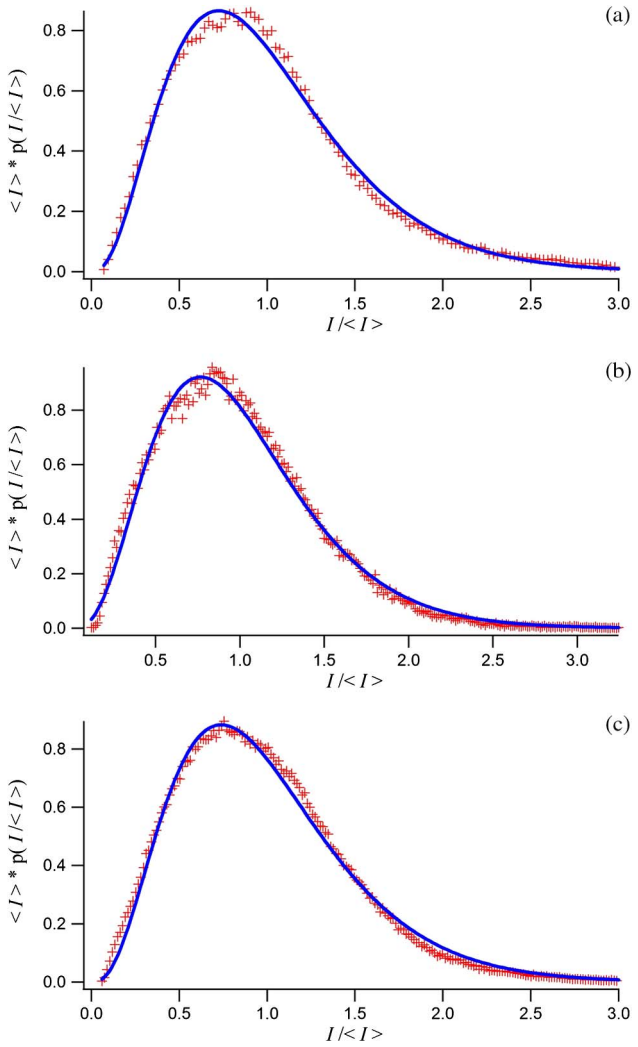

Fig. 10. (Color online) Fits to the Gamma function of Eq. (23) for the image within the orange (left), green (squares), and blue (right) boxes in Fig. 7, corresponding to (a), (b), and (c) here.

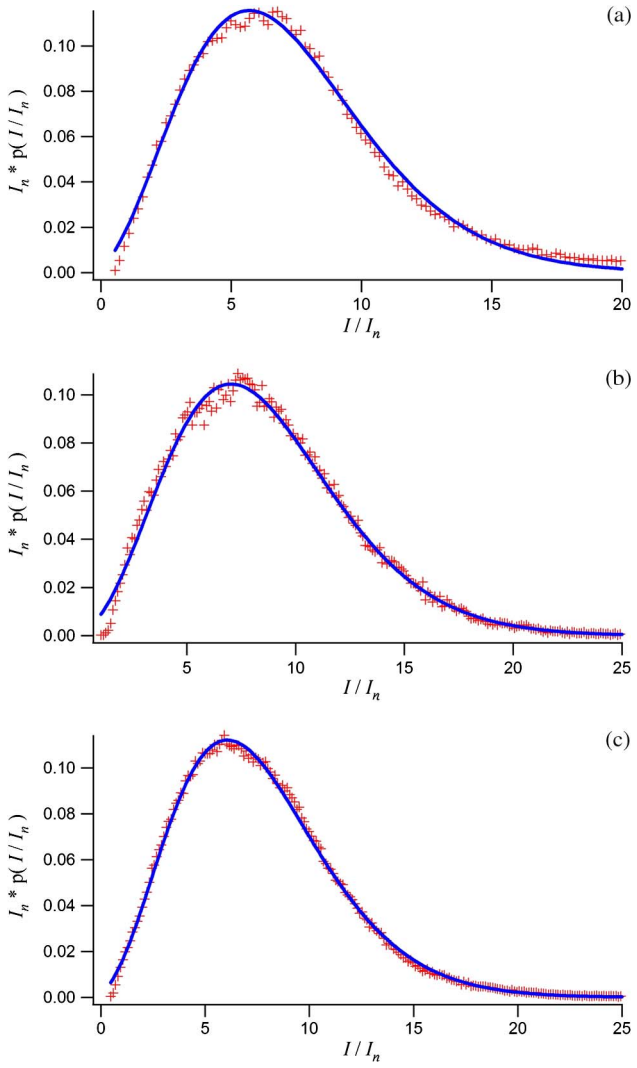

Fig. 11. (Color online) Fits to the Rician function of Eq. (24) for the image within the orange (left), green (squares), and blue (right) boxes of the upper panel in Fig. 7, corresponding to (a), (b), and (c) here.

$$p_I(I) = \frac{1}{I_n} e^{-\left(\frac{I}{I_n}+r\right)} I_0\left(2\sqrt{\frac{I}{I_n} r}\right), \tag{24}$$

where I is the intensity, I_n is the average speckle intensity, r is the ratio of the specular reflection amplitude to the average speckle intensity, and I_0 is the modified Bessel function of order zero. The contrast of the image is

$$C = \frac{\sqrt{1+2r}}{1+r}. \tag{25}$$

The same intensity distributions as above were fit to modified Rician density functions after normalizing to the average speckle intensity, shown in Fig. 11, producing values of $r = 6.2$, 7.5, and 6.6, or an average contrast value of $C = 0.49$.

Inspection of the fits in Figs. 10 and 11 show somewhat better fits for the Rician function, especially in the bottom two panels.

4. Mode-Mixed Image of a Complex Object—the Atrium of the OSU Physics Building

The image in the lower panel of Fig. 7 was taken with the modulated mode mixing illumination on. The result of the modulation is to average together speckle patterns from many illumination modes, as in the averaged knife picture, without having to make many images. The same three regions of the picture as the unmodulated picture were taken for statistical analysis of the speckle. Fitting the intensity distribution to the gamma density function, shown in Fig. 12, the image in the orange box on the left side of the image returned $N = 49.9$, in the green box in the lower middle $N = 158.0$, and in the blue box in the upper right $N = 42.5$. The average contrast value for all three sections of the picture was $C = 0.125$, with the speckle pattern in the green box being reduced by nearly a factor of 2 over the other two regions.

This large number of statistically independent images (and the related large improvement in speckle contrast) is perhaps at first consideration surprising. Our mode mixer rotates at ~100 Hz and considering the two facets of its reflective surface produces a modulation frequency of ~200 Hz. Since our

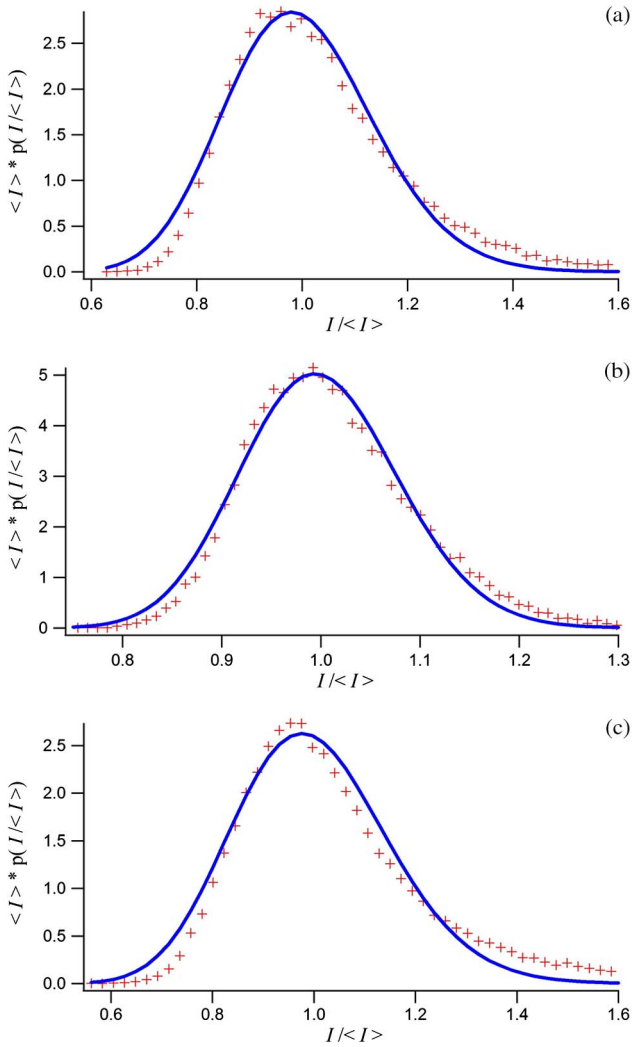

Fig. 12. (Color online) Fits to the Gamma function of Eq. (23) for the averaged image within the orange left), green (squares), and blue (right) boxes in the lower panel of Fig. 7, corresponding to (a), (b), and (c) here.

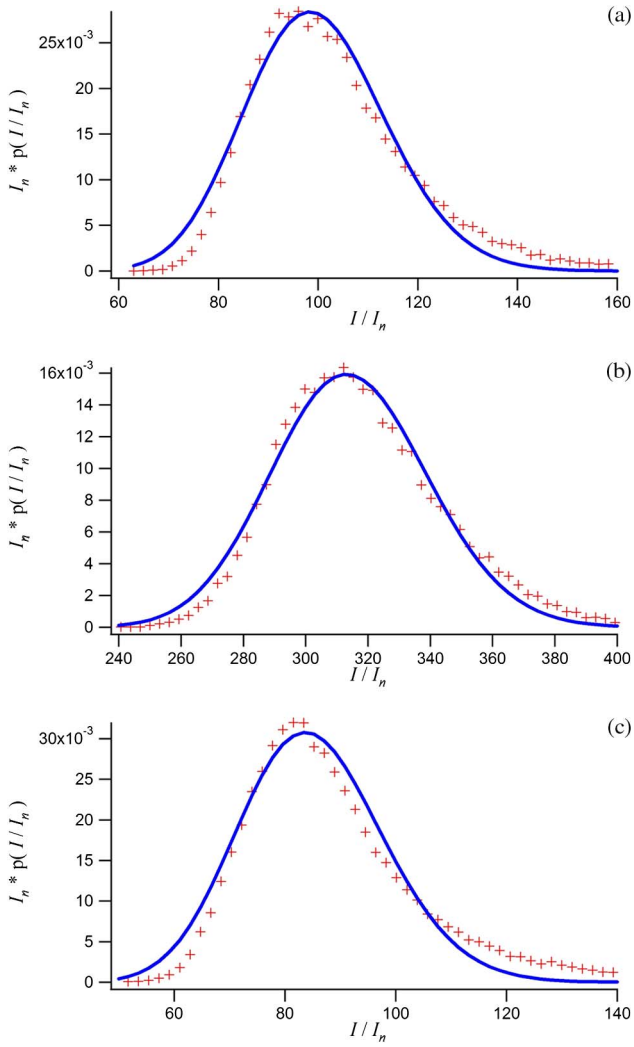

Fig. 13. (Color online) Fits to the Rician function of Eq. (24) for the mode mixed image within the orange (left), green (squares), and blue (right) boxes in the lower panel of Fig. 7, corresponding to (a), (b), and (c) here.

pixel dwell time is of ~10 ms, this is only about two modulation periods per pixel. To achieve the improvements in speckle contrast that we observed, the mode mixer must be illuminating many modes per revolution.

The same three regions were also fit to the modified Rician density function, shown in Fig. 13. In the limit of small contrast, or high N and r, the gamma density function of Eq. (23) and the modified Rician density function of Eq. (24) are nearly indistinguishable; both distributions become Gaussian-like as the speckle contrast approaches 0. The orange box in the middle left returned $r = 98.8$, the green box in the lower middle $r = 315.6$, and the blue box in the upper right $r = 84.2$. The averaged speckle contrast value of the three sections of the picture was $C = 0.124$.

Figure 14 shows the intensity distribution for the region enclosed by the red box in comparison with the intensity distribution enclosed by the green box for the unmodulated picture. The red curve has a much longer tail than the green curve due to the presence of bright specular reflections in the image. Neither the Gamma nor the Rician fit adequately describe the red intensity distribution because of the nonconstant geometry contained in the red box. Both fit functions assume a constant geometry of the target object. Since a more constant geometry produces better fits, it is not surprising that the fits of the knife pictures match experimental data closer than the fits of the atrium pictures.

5. Overview

Regardless of the method of statistical analysis used, the results are very similar, as predicted by the theory itself.

1. As would be expected, regions from the complex image of the atrium show less fully developed speckle than areas selected from the cloth near the knife. Because the cloth was not backed by any reflective material, the fraction of the reflection that is diffuse should be very high. In contrast, much of the atrium is drywall, whose refection contains a significant specular component.

2. For regions selected from the unaveraged images of Fig. 7, the Rician fits (which allow for a combination of specular and diffuse reflection) showed a somewhat better fit than the Gamma fits, with small variation according to region.

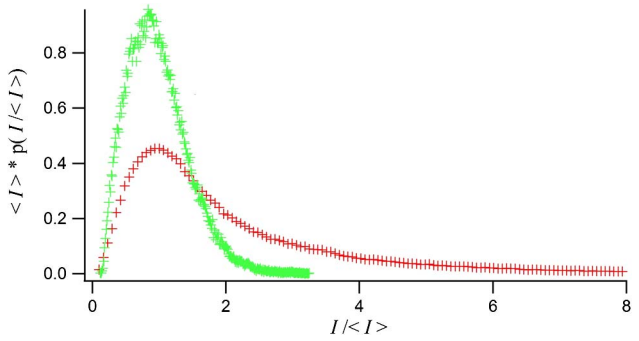

Fig. 14. (Color online) Intensity distributions for the image without mode modulation. The red (lower) curve is the intensity distribution from the red box with specular and diffuse reflections. The green (upper) curve is from the green box with mostly diffuse reflections.

3. Both the Rician and Gamma fits confirmed large reduction in speckle contrast constants of between 6.5 and 12.5.

7. ILLUMINATION STRATEGIES—DISTANT TARGETS

In Section 4 we considered the "hot blackbody" illumination limit and in Section 6 we showed experimental results that were close to this limit. We also noted that there were alternative illuminations strategies, especially for distant or unenclosed targets, such as the urban canyon shown in Fig. 15. Here we discuss some of these strategies in the context of an $n \times n$ array, which for numerical examples will be assumed $n = 100$, a scale of $l = 100$ m, and observing optics for which $D_o = 1$ m.

For these alternative illumination strategies two principal issues will be considered: (1) the amount of reduction in speckle contrast that can be obtained and (2) the efficiency of the use of the illumination photons.

A. Signal Strengths

As above, we assume that scattering from a diffuse surface uniformly illuminates a hemisphere and that the scattering reflections are small enough that multiple reflections are not significant. As we have noted, in a single mode of bandwidth 1 MHz, 1 mW, and 10 W correspond to 10^{14} K and 10^{18} K, respectively.

Direct illumination mode: If we assume that all of the transmit power that directly illuminates a single pixel with a reflectivity $R_t = 0.1$ at 100 m is uniformly scattered into the viewing hemisphere, an antenna of diameter $D_o = 1$ m will view modes with brightness temperatures of $\frac{10^9\ \mathrm{K}}{2\pi}$ or $\frac{10^{13}\ \mathrm{K}}{2\pi}$, respectively. If these illumination powers are distributed over an $n \times n$ array, with $n = 100$, these temperatures are reduced by the number of pixels that share the illumination and become $\frac{10^5\ \mathrm{K}}{2\pi}$ or $\frac{10^9\ \mathrm{K}}{2\pi}$, respectively.

Indirect illumination mode: Above in Section 4, we considered the uniform illumination of a volume of scale $l = 100$ m to produce a very hot blackbody. For our two example illuminator powers we found that the target temperatures in the receiver modes were $\frac{10^2\ \mathrm{K}}{4\pi^2}$ and $\frac{10^6\ \mathrm{K}}{4\pi^2}$. Let us next consider another indirect illumination mode that has close analogy to optical floodlight illumination. In this approach we illuminate a scattering surface near the target, rather than the entire surface of a scattering volume. This calculation is appropriate for the geometry shown in Fig. 15. If this scattering surface has a reflectivity of R_s, is a distance r_{st} from the target that lies on a hemisphere centered at the scattering surface; and if $r_{st} \neq r_{to} = l$, for $r_{st} = 20$ m the reduction in target temperature from the direct illumination mode of Section 4 becomes $\frac{2\pi D_o^2}{n^2\lambda^2 R_s}\frac{r_{ts}^2}{r_{to}^2} = 80\pi$ and the temperature in the receiver modes becomes for our two illumination examples $\frac{25\cdot 10^2\ \mathrm{K}}{4\pi^2}$ and $\frac{25\cdot 10^6\ \mathrm{K}}{4\pi^2}$. The lower target temperature results from the assumed illumination scattering loss of $R_s = 0.1$ and from the fraction of the 2π solid angle that the $n \times n$ target fills as viewed by the scattering illumination surface. Alternatively, in comparison to the illumination of the entire volume, these temperatures are larger by $(l/r_{st})^2$, in our case 25. Table 1 summarizes these results.

Phased array illumination: In an ideal case where all of the multimode illumination is delivered to all of the pixels all of the time, but from n^2 modulated modes, no photons are wasted. This can be accomplished by an $n \times n$ phased array of transmit antennas. If these antennas are spaced by the diameter D_o of the imaging antenna, then n^2 illumination modes with independent illumination modes would result and their modulation would reduce the speckle contrast by n. In the case of $n = 100$, the speckle contrast would be reduced by 100. However, to achieve this favorable result, the illuminators would have to be spaced over a $nD_o \times nD_o$ (100 m × 100 m) area. While this may be awkward, this is perhaps an interesting configuration for a phased array that does not seek a speckle reduction of the full factor of 100, especially since the size of each of the transmit antennas need only be D/n, in our example 1 cm. In this case there are no wasted

Fig. 15. (Color online) Conceptual urban canyon application (courtesy M. Rosker).

Table 1. Comparison of Illumination Temperatures

	1 mW Illumination	10 W Illumination
Direct illumination	$\frac{10^5\ \mathrm{K}}{2\pi} = 1.59 \cdot 10^4$ K	$\frac{10^9\ \mathrm{K}}{2\pi}$
Full blackbody illumination	$\frac{10^2\ \mathrm{K}}{4\pi^2} = 2.5$ K	$\frac{10^6\ \mathrm{K}}{4\pi^2} = 25000$ K
Indirect illumination $r_{st} = 20$ m	$\frac{25\cdot 10^2\ \mathrm{K}}{4\pi^2} = 62.5$ K	$\frac{25\cdot 10^6\ \mathrm{K}}{4\pi^2} = 625000$ K

photons and receiver mode temperatures the same as for the direct, non-mode-mixed illumination would result, but in a configuration that allows for speckle reduction.

B. Size of Speckle Reduction Factor

We have seen that speckle reduction can be accomplished by the illumination of the target by sources with uncorrelated phase and that the maximum reduction in speckle contrasts is $\sqrt{\frac{1}{N}}$, where N is the number of modes, as defined by the imaging (not illuminating) optics.

In an enclosure of scale $l = 100$ m,

$$N = \frac{2\pi r^2}{D_0^2} = 2\pi \cdot 10^4. \tag{26}$$

For a scattering area D_s^2 and $r_{st} = 20\,m.$,

$$N = \left(\frac{D_s}{D_0}\right)^2 = 400. \tag{27}$$

Note that D_s matters for speckle reduction, but not in the signal strength—a free variable, but limited by $D_s \le r_{st}$, equating these two leads to $N = 10^4$. The similarity of these two numbers reflects that the scattering surface fills a significant fraction of the solid angle viewed by the target.

8. CONCLUSIONS

We have demonstrated in a large volume a general active imaging method based on modulated mixings of many illumination modes that significantly reduces coherent effects (such as speckle). It also eliminates the need for the strategic target orientation typical of many demonstrations of active imaging. The resultant images have many of the favorable characteristics of passive images, but with orders of magnitude greater brightness temperatures. We have also considered alternative floodlight illumination strategies that have close analogy to optical indirect lighting and which are applicable at considerable (~1 km) range.

More specifically we have shown the following:

(1) To achieve a significant reduction in the speckle contrast, the target must be illuminated from many modes, with the speckle reduction factor being $N^{1/2}$, where N is the number of independent modes.

(2) Large values of N (>100) can be obtained with simple mode mixing strategies.

(3) This approach is made practical by the high brightness temperatures (10^{14}–10^{18} K) that can be attained with narrowband electronic illuminators.

(4) Because of this high brightness, this approach can be implemented by scattering from surfaces of large volumes (e.g., ~100 m in arenas or atriums) or for larger (~1 km) and outdoor applications by more directed illumination strategies.

(5) While filling many modes with illumination can be relatively wasteful of photons, the illumination of a scattering surface reasonably close to the target is an efficient and attractive approach. In this case, because the target can fill a substantial fraction of the solid angle illuminated by this scattering, the illumination photons are relatively efficiently used.

(6) The scattering illumination is much more efficient for use with focal plane arrays because the entire target collects a much larger fraction ($\times 10^4$) of the photons from a scattering surface than does a single pixel.

(7) For room-temperature operation, the required detector sensitivity is best obtained in narrow bandwidth, heterodyne receivers. The higher powers associated with vacuum electronic sources are capable of supplying the required local oscillator power to large arrays.

(8) For the longer ranges and to broaden the range of scenarios by reducing the requirements on appropriate scattering surfaces, the powers associated with vacuum electronic are very useful.

ACKNOWLEDGMENTS

We would like to thank the Army Research Office and DARPA for their support of this work.

REFERENCES

1. S. M. Kulpa and E. A. Brown, *Near-Millimeter Wave Technology Base Study* (Harry Diamond Laboratories, 1979).
2. P. W. Kruse, "Why the military interest in near-millimeter wave imaging?" Proc. SPIE **259**, 94–97 (1980).
3. D. M. Sheen, D. L. McMakin, and T. E. Hall, "Three-dimensional millimeter-wave imaging for concealed weapon detection," IEEE Trans. Microwave Theor. Tech. **49**, 1581–1592 (2001).
4. E. N. Grossman, A. Luukanen, and A. J. Miller, "Terahertz active direct detection imagers," Proc. SPIE **5411**, 68–77 (2004).
5. A. Luukanen, A. J. Miller, and E. N. Grossman, "Active millimeter-wave video rate imaging with a staring 120-element microbolometer array," Proc. SPIE **5410**, 195–210 (2004).
6. D. T. Petkie, C. Casto, F. C. De Lucia, S. R. Murrill, B. Redman, R. L. Espinola, C. C. Franck, E. L. Jacobs, S. T. Griffin, C. E. Halford, J. Reynolds, S. O'Brien, and D. Tofsted, "Active and passive imaging in the THz spectral region: phenomenology, dynamic range, modes, and illumination," J. Opt. Soc. Am. B **25**, 1523–1531 (2008).
7. I. Ocket, D. Schreurs, V. Tavakol, F. Qi, B. Nauwelaers, and J. Stiens, "Design challenges for millimeter wave active imaging systems," in *Proceedings of the 7th European Radar Conference* (IEEE, 2010), pp. 312–315.
8. S. Yeom, D.-S. Lee, J.-Y. Son, M.-K. Jung, Y. Jang, S.-W. Jung, and S.-J. Lee, "Real-time outdoor concealed-object detection with passive millimeter wave imaging," Opt. Express **19**, 2530–2536 (2011).
9. L. Zhang, J. Stiens, A. Elhawil, and R. Vounckx, "Multispectral illumination and image processing techniques for active millimeter-wave concealed object detection," Appl. Opt. **47**, 6357–6365 (2008).
10. I. Jaeger, J. Stiens, L. Zhang, S. Islam, G. Koers, and R. Vounckx, "Comparison of speckle reduction diversity tools for active millimeter-wave imaging," J. Opt. Soc. Am. A **25**, 1716–1721 (2008).
11. G. Koers, I. Ocket, Q. Feng, V. Tavakol, I. Jäger, B. Nauwelaers, and J. Stiens, "Study of active millimeter-wave image speckle reduction by Hadamard phase pattern illumination," J. Opt. Soc. Am. A **25**, 312–317 (2008).
12. D. N. Bittner, R. L. Crownover, F. C. De Lucia, and S. L. Shostak, "Passive imaging with a broadband cooled detector," in *12th International Conference on Infrared and Millimeter Waves* (IEEE, 1987).
13. H. B. Wallace, "Analysis of RF imaging applications at frequencies over 100 GHz," Appl. Opt. **49**, E38–E47 (2010).
14. Y.-W. Chang and M. Johnson, "Portable concealed weapon detection using millimeter wave FMCW radar imaging," Proc. SPIE **4232**, 134–141 (1998).
15. W. Caba and G. D. Boreman, "Active sparse-aperture millimeter-wave imaging using digital correlators," J. Infrared Millim. Terahertz Waves **32**, 434–450 (2011).

16. C. am Weg, W. von Spiegel, R. Henneberger, R. Zimmermann, T. Loeffler, and H. G. Roskos, "Fast active THz cameras with ranging capabilities," J. Infrared Millim. Terahertz Waves **30**, 1281–1296 (2009).
17. T. D. Dorney, W. W. Symes, R. G. Baraniuk, and D. M. Mittleman, "Terahertz multistatic reflection imaging," J. Opt. Soc. Am. **19**, 1432–1442 (2002).
18. Q. Li, S.-H. Ding, R. Yao, and Q. Wang, "Real-time terahertz scanning imaging by use of a pyroelectric array camera and image denoising," J. Opt. Soc. Am. **27**, 2381–2386 (2010).
19. T. W. Du Bosq, J. M. Lopez-Alonso, and G. D. Boreman, "Millimeter wave imaging system for land mine detection," Appl. Opt. **45**, 5686–5692 (2006).
20. D. T. Petkie, J. Holt, M. A. Patrick, and F. C. De Lucia, "Multimode illumination in the terahertz for elimination of target orientation requirements and minimization of coherent effects in active imaging systems," Opt. Eng. **51**, 091604 (2012).
21. K. B. Cooper, R. J. Denglera, N. Llombartb, A. Talukdera, A. V. Panangadana, C. S. Peaya, I. Mehdia, and P. H. Siegel, "Fast, high-resolution terahertz radar imaging at 25 meters," Proc. SPIE **7671**, 76710Y (2010).
22. W. B. Lewis, "Fluctuations in streams of thermal radiation," Proc. Phys. Soc **59**, 34–40 (1947).
23. E. H. Putley, "The ultimate sensitivity of sub-mm detectors," Infrared Phys. **4**, 1–8 (1964).
24. F. C. De Lucia, "Noise, detectors, and submillimeter-terahertz system performance in nonambient environments," J. Opt. Soc. Am. B **21**, 1273–1297 (2004).
25. E. Grossman, C. Dietlein, J. Ala-Laurinaho, M. Leivo, L. Gronberg, M. Gronholm, P. Lappalainen, A. Rautiainen, A. Tamminen, and A. Luukanen, "Passive terahertz camera for standoff security screening," Appl. Opt. **49**, E106–E120 (2010).
26. N. George and A. Jain, "Speckle reduction using multiple tones of illumination," Appl. Opt. **12**, 1202–1212 (1973).
27. N. George, A. Jain, and R. D. S. Melville, Jr., "Experiments on the space and wavelength dependence of speckle," Appl. Phys. **7**, 157–169 (1975).
28. J. W. Goodman, "Dependence of image speckle contrast on surface roughness," Opt. Commun. **14**, 324–327 (1975).
29. J. W. Goodman, "Some fundamental properties of speckle," J. Opt. Soc. Am. **66**, 1145–1150 (1976).
30. J. W. Goodman, *Speckle Phenomena in Optics: Theory and Applications* (Roberts, 2007).
31. N. George, C. R. Christensen, J. S. Bennett, and B. D. Guenther, "Speckle noise in displays," J. Opt. Soc. Am. **66**, 1282–1290 (1976).
32. A. Yariv, *Quantum Electronics*, 2nd ed. (Wiley, 1975).
33. P. Coward and R. Appleby, "Development of an illumination chamber for indoor millimetre-wave imaging," Proc. SPIE **5077**, 54–61 (2003).
34. N. E. Alexander, C. C. Andres, and R. Gonzalo, "Multispectral mm-wave imaging: materials and images," Proc. SPIE **6948**, 694803 (2008).
35. F. Qi, V. Tavakol, D. Schreurs, and B. Nauwelaers, "Limitations of approximations towards Fourier optics for indoor active millimeter wave imaging systems," Prog. Electromagn. Res. **109**, 245–262 (2010).
36. F. Qi, V. Tavakol, I. Ocket, P. Xu, D. Schreurs, J. Wang, and B. Nauwelaers, "Millimeter wave imaging system modeling: spatial frequency domain calculation versus spatial domain calculation," J. Opt. Soc. Am. A **27**, 131–140 (2010).